JOURNAL OF COMPUTATIONAL PHYSICS 3, 226–258 (1968)

A Discrete Eulerian Model of Spherically Symmetric Compressible Media*

E. FACCIOLI

International Center of Earthquake Engineering, Politecnico di Milano, Milano, Italy

AND

A. H.-S. ANG

Professor of Civil Engineering, University of Illinois, Urbana, Illinois 61801

Received July 1, 1968

ABSTRACT

A discrete Eulerian model is described through which a set of centered finite difference equations for spherical media can be derived on the basis of clear physical principles, namely, the explicit conservation of mass, momentum, and energy. A solution procedure is proposed, and the associated stability study is presented. The method is illustrated for several problems of wave and shock propagation of earth media subjected to pressure pulses.

I. INTRODUCTION

Studies of the dynamic response of earth media to buried and surface explosive forces, particularly to nuclear explosives, have lately multiplied at an increasing rate. Because of the limitations of analytic solutions, much of these efforts have been directed to the development of numerical methods for high-speed computation. A primary consideration in such studies is the assurance of convergence of the numerical solutions to the corresponding true solutions, although too often this consideration is overlooked. In the absence of an exact solution for evaluating the validity of a numerical scheme, questions of convergence and error propagation are indeed difficult to answer.

However, if a problem is formulated through a discrete conceptual model, the lack of guidance provided by exact solutions can be partially compensated by requiring that the model equations be derived making maximum use of the physical principles leading to the exact continuum equations. For example, if it is desired

* This work was supported by the National Science Foundation under grant NSF-GK 589.

to derive a discrete cell-analogue of the Eulerian conservation principles in integral form, such an analogue should be based on the explicit conservation of mass, momentum, and energy. Not only does this approach have the advantage of providing a clear picture of the physical principles involved, it also cast more light on the source of the discretization errors of the model equations. This point of view is not new; its importance was perhaps first pointed out by Lax [3]. However, it has not always been consistently applied or thoroughly exploited, except in the Lagrangian treatment of small distortion propagation problems in solids [2]. An Eulerian model is presented here for the discrete formulation of spherically symmetric problems using this approach.

To the knowledge of the authors, practically all of the existing Eulerian numerical schemes ([3], [4], [5], [6]) were developed to describe wave propagation in the hydrodynamic regime, where material distortions are so large as to render a purely Lagrangian treatment either impractical or unfeasible. There might equally be good reasons also for using an Eulerian cell-analogue approach for describing the dynamic environment under low stress levels. For example, in the consideration of the effects of nuclear explosions in soil media, the material distortions may be large even in the ranges where the state of stress is below the hydrodynamic range. Furthermore, the results of certain Lagrangian techniques appear to contain undesirable features; see, for instance, the "noise" in the results described in [7] which may not be totally attributable to questions of stability. This poses the question of whether an Eulerian treatment might not have intrinsic advantages as far as the smoothness of the calculations is concerned.

A serious difficulty associated with any Eulerian approach is the presence of a moving boundary, such as the problem of an expanding cavity considered herein. This difficulty can be resolved through a consistent use of the conservation statements, coupled with a suitable extrapolation procedure, which allows the boundary to move through the Eulerian grid in a smooth and continuous manner.

A linear stability analysis of the interior difference equations indicates that the two-step numerical scheme devised for advancing the solution in the space-time domain can be made conditionally stable by introducing appropriate artificial viscosity terms of the linear type. Also, a comparison with an available exact solution in the small deformation range shows that the numerical results converge to the analytic solution as the space mesh is reduced.

Two large-deformation problems are illustrated; one of these involves elastic-plastic wave propagation in granite, and the other is concerned with shock propagation in playa silt.

Although the model is described primarily for low stress wave propagation in solid media under isentropic conditions of flow, it can be easily adapted for purely hydrodynamic conditions, such as occuring in the close-in region of a nuclear explosion.

Integral Form of the Continuum Conservation Principles

Consider an idealized medium in which no viscous friction and no heat conduction can occur. If the Eulerian viewpoint is adopted, the conservation principles may be stated with reference to a finite "control volume" fixed in space, through which the medium is supposed to flow without discontinuities. Neglecting the action of body forces, the conservation equations read as follows:

$$\int_\tau \frac{\partial \rho}{\partial t}\, d\tau + \int_S \bar{m} \cdot \bar{n}\, dS = 0, \qquad \text{(conservation of mass)} \tag{1}$$

$$\int_\tau \frac{\partial \bar{m}}{\partial t}\, d\tau + \int_S \frac{\bar{m}^2}{\rho} \cdot \bar{n}\, dS = \int_S f\bar{n}\, dS, \qquad \text{(conservation of momentum)} \tag{2}$$

$$\int_\tau \frac{\partial e}{\partial t}\, d\tau + \int_S e\frac{\bar{m}}{\rho} \cdot \bar{n}\, dS = \int f\frac{\bar{m}}{\rho} \cdot \bar{n}\, dS, \qquad \text{(conservation of total energy)} \tag{3}$$

where:

ρ, $\bar{m}$ and e are the mass, momentum, and total energy per unit volume;
f is the surface traction acting on a unit area of the generic surface;
τ is the control volume bounded by the surface S; and
$\bar{n}$ is the outward normal of S.

In each of the above equations, the first integral on the left side can be interpreted as the time rate of accumulation of the respective total quantity (mass, momentum, energy) that is being conserved; let this quantity be denoted by B. The second integral on the left side represents the algebraic difference between the outflux and the influx of B through S. The integral on the right side of Eq. (2) is the total force exerted on τ through S by the surrounding medium, whereas the corresponding integral in Eq. (3) is the rate of work performed on S by the surface traction f. Any dissipative mechanism within τ is clearly ignored in Eq. (3).

Consider now a control volume with spherical geometry, as shown in Fig. 1, and assume that the flow occurs only through S_1 and S_2, in the directions normal to these surfaces as indicated by the arrows. If there is complete radial symmetry, f, ρ, m, and e are constants on S_1 and on S_2. Under these conditions and applying the law of the mean of the volume integrals, Eqs. (1) through (3) reduce, respectively, to

$$\left[\frac{\partial \rho}{\partial t}\right]_Q \tau = m_1 A_1 - m_2 A_2, \tag{4}$$

$$\left[\frac{\partial m}{\partial t}\right]_Q \tau = (m^2/\rho)_1 A_1 - (m^2/\rho)_2 A_2 + F_\tau, \tag{5}$$

$$\left[\frac{\partial e}{\partial t}\right]_Q \tau = [(e - f)\, m/\rho]_1 A_1 - [(e - f)\, m/\rho]_2 A_2, \tag{6}$$

where:

F_r is the radial component of the total force $\int_S f\bar{n}\, dS$;

A_1 and A_2 are the areas of S_1 and S_2, respectively.

The subscripts 1 and 2 denote the constant value taken by the flow quantities on S_1 and S_2. Also, $[\ ]_Q$ indicates that the time derivatives are evaluated at a proper point Q in τ.

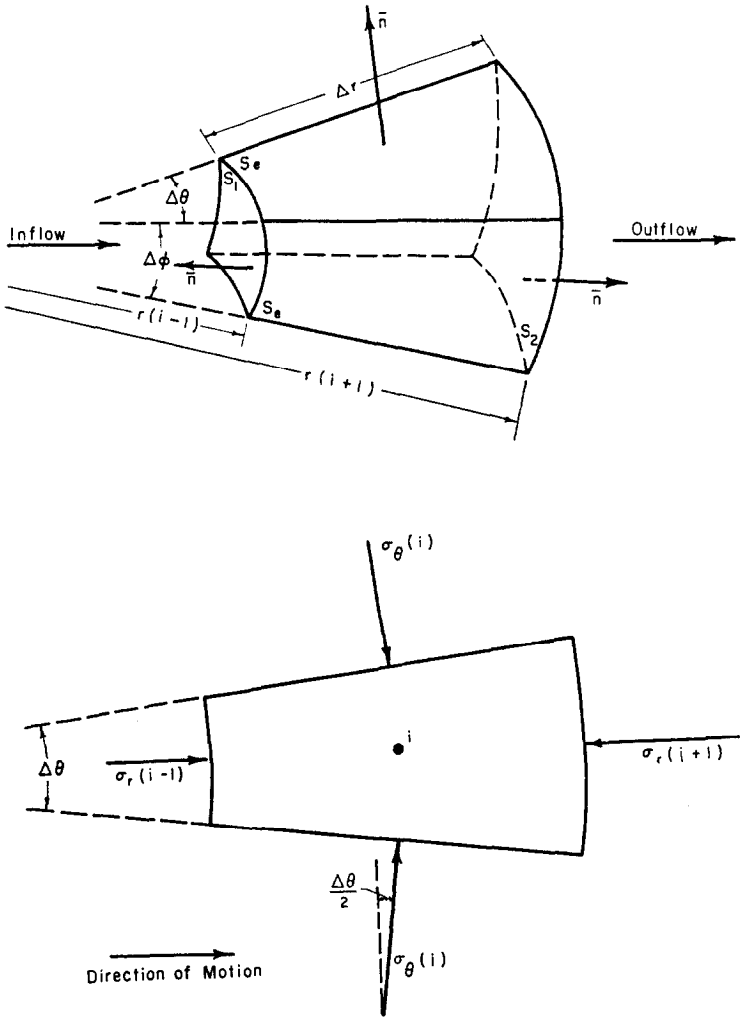

FIG. 1. Spherically symmetric Eulerian cell.

It should be clear that, dividing throughout by τ and letting $\tau \to 0$ in Eqs. (4) through (6), the continuum equations of spherically symmetric compressible flow in conservative form are obtained.

II. Description of the Model

Conservation Equations for General Interior Cell

In the discrete cell-analogue model proposed herein, a spherically symmetric cell of finite dimensions and of fixed position in space is taken as the elemental unit in which the basic conservation requirements are to be satisfied (Fig. 1).

The relevant field quantities are defined only at the center of each cell and

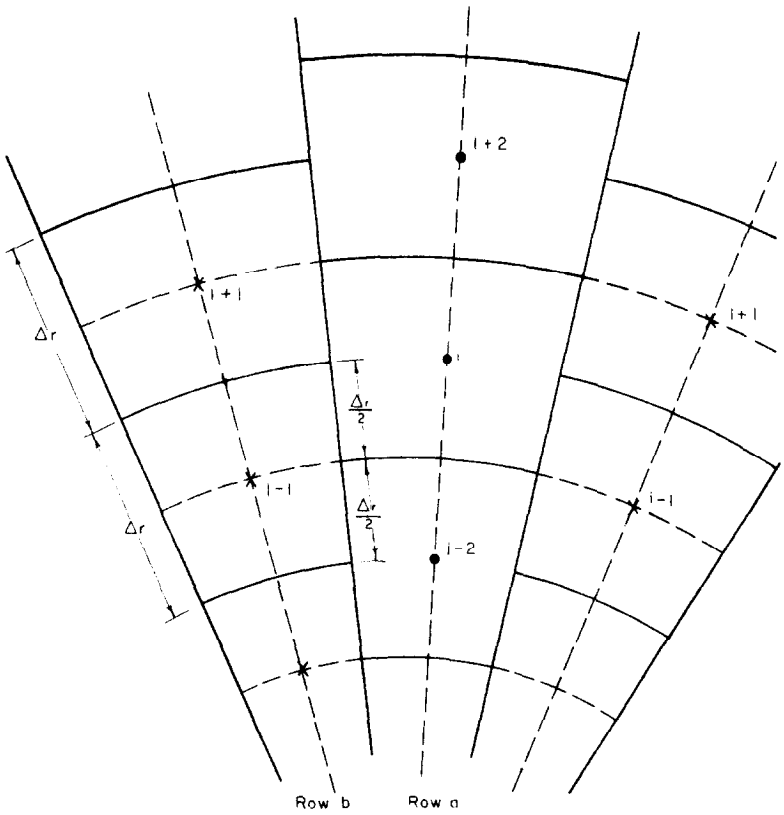

Fig. 2. Cross section of spherical model.

represent average values in the volume of the cell. It is clear that conservation requirements concerning a single cell will depend on the flow of the material across its boundaries, and therefore on the definition of the field values associated with the mass transport from cell to cell. For this purpose, consider the staggered array of cells shown for a cross section of the spherical model of Fig. 2. Because of the assumption of spherical symmetry, the field quantities at the boundary of a cell in a given row (e.g. row "a" in Fig. 2) are equal to the corresponding quantities defined at the center of the adjacent cell (e.g. in row "b").

Assuming a discrete time variable, the conservation statements for a cell i over a finite time interval Δt, are as follows:

$$M(i, t + \Delta t) = M(i, t) + \Delta M_I(i - 1) - \Delta M_0(i + 1), \quad \text{(conservation of mass)} \tag{7}$$

$$T(i, t + \Delta t) = T(i, t) + \Delta T_I(i - 1) - \Delta T_0(i + 1) + \Delta I(i), \quad \text{(conservation of momentum)} \tag{8}$$

$$H(i, t + \Delta t) = H(i, t) + \Delta H_I(i - 1) - \Delta H_0(i + 1) + \Delta W(i), \quad \text{(conservation of total energy)} \tag{9}$$

where:

$M(i, t)$, $T(i, t)$ and $H(i, t)$ are the total mass, momentum and energy in cell i at time t;

$\Delta M_I(i - 1)$, $\Delta T_I(i - 1)$ and $\Delta H_I(i - 1)$ are the mass, momentum and energy of the material flowing into cell i during the interval Δt;

$\Delta M_0(i + 1)$, $\Delta T_0(i + 1)$ and $\Delta H_0(i + 1)$ are the mass, momentum and energy of the material flowing out of cell i during Δt;

$\Delta I(i)$ is the change of impulse on cell i during Δt; and

$\Delta W(i)$ is the net work performed during Δt by the forces acting on the boundaries of cell i at time t.

Consider first the conservation of momentum, Eq. (8), and let

$$T(i, t + \Delta t) = m(i, t + \Delta t)\, \tau(i); \qquad T(i, t) = m(i, t)\, \tau(i)$$

where (see Fig. 1)

$$\tau(i) = \int_{-\Delta\theta/2}^{\Delta\theta/2} d\theta \int_{-\Delta\varphi/2}^{\Delta\varphi/2} d\varphi \int_{r(i)-\Delta r/2}^{r(i)+\Delta r/2} r^2\, dr = r^2(i)[1 + \Delta r^2/12r^2(i)] \cong r^2(i)\, \Delta r\, \Delta\varphi\, \Delta\theta$$

assuming that the term $\Delta r^2/12r^2(i)$ is negligible in comparison with unity. Furthermore, the transport term $\Delta T_I(i-1)$ can be expressed as

$$\Delta T_I(i-1) = \int_{-\Delta\theta/2}^{\Delta\theta/2} d\theta \int_{-\Delta\varphi/2}^{\Delta\varphi/2} d\varphi \int_t^{t+\Delta t} [m^2(i-1,\zeta)/\rho(i-1,\zeta)]\, r^2(i-1)\, d\zeta$$
$$= [m^2(i-1,t^*)/\rho(i-1,t^*)]r^2(i-1)\Delta t\, \Delta\varphi\, \Delta\theta,$$
$$t \leqslant t^* \leqslant t + \Delta t.$$

Analogously,

$$\Delta T_0 = [m^2(i+1,t^{**})/\rho(i+1,t^{**})]r^2(i+1)\Delta t\, \Delta\varphi\, \Delta\theta, \qquad t \leqslant t^{**} \leqslant t + \Delta t$$

The change of impulse $\Delta I(i)$ can also be written as

$$\Delta \mathrm{I}(i) = \int_t^{t+\Delta t} F_r(i,t) = F_r(i,\bar{t})\, \Delta t; \qquad t \leqslant \bar{t} \leqslant t + \Delta t. \tag{10}$$

If a hydrodynamic state of stress p is considered and the forces acting on the cell boundary are taken as positive in the direction of increasing r, the change of impulse is

$$\Delta I(i) = [p(i-1,\bar{t})\, r^2(i-1) - p(i+1,\bar{t})\, r^2(i+1)]\, \Delta t\, \Delta\varphi\, \Delta\theta$$
$$+ 2p(i,\bar{t})\, r(i) \sin\frac{\Delta\theta}{2}\, \Delta r\, \Delta\varphi\, \Delta t + 2p(i,\bar{t})\, r(i) \sin\frac{\Delta\varphi}{2}\, \Delta r\, \Delta\theta\, \Delta t$$
$$\cong [p(i-1,\bar{t})\, r^2(i-1) - p(i+1,\bar{t})\, r^2(i+1)]\, \Delta t\, \Delta\varphi\, \Delta\theta$$
$$+ 2p(i,\bar{t})\, r(i)\, \Delta r\, \Delta\varphi\, \Delta\theta\, \Delta t,$$

in which $\Delta\varphi$ and $\Delta\theta$ are regarded as small angles. If a nonhydrodynamic stress description is required, with a radial component σ_r and two tangential components $\sigma_\theta = \sigma_\varphi$, the above impulse term then becomes (see Fig. 1):

$$\Delta I(i) = [\sigma_r(i-1,\bar{t})\, r^2(i-1) - \sigma_r(i+1,\bar{t})\, r^2(i+1)]\, \Delta t\, \Delta\varphi\, \Delta\theta$$
$$+ 2\sigma_\theta(i,\bar{t})\, r(i)\, \Delta r\, \Delta\varphi\, \Delta\theta\, \Delta t.$$

Substituting the above expressions of T, ΔT and ΔI into Eq. (8) and neglecting terms of order $O(\Delta r^2/r^2)$, the following equation is obtained:

$$m(i,t+\Delta t) = m(i,t) + \frac{\Delta t}{\Delta r}[p(i-1,\bar{t}) + m^2(i-1,t^*)/\rho(i-1,t^*) - p(i+1,\bar{t})$$
$$- m^2(i+1,t^{**})/\rho(i+1,t^{**})] - \frac{\Delta t}{r(i)}[m^2(i-1,t^*)/\rho(i-1,t^*)$$
$$+ m^2(i+1,t^*)/\rho(i+1,t^*)] + \frac{\Delta t}{r(i)}[2p(i,\bar{t}) - p(i-1,\bar{t})$$
$$- p(i+1,\bar{t})] \tag{11}$$

for the hydrodynamic case; whereas for the nonhydrodynamic case the corresponding equation is,

$$m(i, t + \Delta t) = m(i, t) + \frac{\Delta t}{\Delta r}[\sigma_r(i - 1, \bar{t}) + m^2(i - 1, t^*)/\rho(i - 1, t^*) - \sigma_r(i + 1, \bar{t}) - m^2(i + 1, t^{**})/\rho(i + 1, t^{**})] + \frac{\Delta t}{r(i)}[2\sigma_\theta(i, \bar{t}) - \sigma_r(i - 1, \bar{t}) - m^2(i - 1, \bar{t})/\rho(i - 1, \bar{t}) - \sigma_r(i + 1, \bar{t}) - m^2(i + 1, \bar{t})/\rho(i + 1, \bar{t})]. \tag{12}$$

In the limit, when $\Delta t \to 0$ and $\Delta r \to 0$, Eqs. (11) and (12) yield, respectively,

$$\frac{\partial m}{\partial t} = -\frac{\partial(p + m^2/\rho)}{\partial r} - \frac{2m^2/\rho}{r} \tag{13}$$

and

$$\frac{\partial m}{\partial t} = -\frac{\partial(\sigma_r + m^2/\rho)}{\partial r} - \frac{2(\sigma_r - \sigma_\theta + m^2/\rho)}{r} \tag{14}$$

Now if the above operations are applied on Eqs. (7) and (9), the following equations are obtained accordingly:

$$\rho(i, t + \Delta t) = \rho(i, t) + \frac{\Delta t}{\Delta r}[m(i - 1, t^*) - m(i + 1, t^{**})] - \frac{\Delta t}{r(i)}[m(i - 1, t^*) + m(i + 1, t^{**})] \tag{15}$$

for the conservation of mass; and

$$\begin{aligned} e(i, t + \Delta t) = e(i, t) &+ \frac{\Delta t}{\Delta r}[e(i - 1, t^*)\, m(i - 1, t^*)/\rho(i - 1, t^*) \\ &+ p(i - 1, \bar{t})\, m(i - 1, \bar{t})/\rho(i - 1, \bar{t}) \\ &- e(i + 1, t^{**})\, m(i + 1, t^{**})/\rho(i + 1, t^{**}) \\ &- p(i + 1, \bar{t})\, m(i + 1, \bar{t})/\rho(i + 1, \bar{t})] \\ &- \frac{\Delta t}{r(i)}[e(i - 1, t^*)\, m(i - 1, t^*)/\rho(i - 1, t^*) \\ &+ p(i - 1, \bar{t})\, m(i - 1, \bar{t})/\rho(i - 1, \bar{t}) \\ &+ e(i + 1, t^{**})\, m(i + 1, t^{**})/\rho(i + 1, t^{**}) \\ &+ p(i + 1, \bar{t})\, m(i + 1, \bar{t})/\rho(i + 1, \bar{t})], \end{aligned} \tag{16}$$

for conservation of total energy. Eq. (16) holds also for the nonhydrodynamic stress case, if p is replaced by σ_r.

Again in the limit as $\Delta t \to 0$ and $\Delta r \to 0$, Eqs. (15) and (16) reduce, respectively, to

$$\frac{\partial \rho}{\partial t} = -\frac{\partial m}{\partial r} - \frac{2m}{r}, \tag{17}$$

and

$$\frac{\partial e}{\partial t} = -\frac{\partial[(p+e)\, m/\rho]}{\partial r} - \frac{2[(p+e)\, m/\rho]}{r}. \tag{18}$$

It is easily recognized that the above equations for the model, Eqs. (11), (15), and (16), are space-centered difference analogues of the corresponding continuum differential equations, Eqs. (13), (17) and (18), respectively. It should be emphasized that Eqs. (11), (15) and (16) explicitly conserve mass, momentum, and total energy per unit volume; this stems from the fact that the elementary conservation requirements for a cell, expressed by Eqs. (7) through (9), are analogues of the integral conservation laws of Eqs. (1) through (3).

The following sources of discretization errors should be recognized. First of all, since Δr cannot be arbitrarily small, the terms of order $O(\Delta r^2/r^2)$ may not be negligible for small r as was assumed in the derivation of the above equations. This may give rise to appreciable errors for problems involving regions where r is small. Also the divergence type term $[2p(i, \bar{t}) - p(i-1, \bar{t}) - p(i+1, \bar{t})]\, \Delta t/r(i)$, which appears in Eq. (11) and vanishes as $\Delta r \to 0$, is likely to produce undesirable errors when very small values of r are involved in the calculations. The same term may also cause spurious diffusion effects when large pressure gradients are acting over a length of less than 2 to 3 mesh lengths.

Another source of possible discretization error is associated with t^*, t^{**}, etc. at which the transport and impulse terms should be evaluated. Since the time is increased by finite steps, the actual distribution of the field functions between generic time instants t and $t + \Delta t$ is not known, nor can it be computed. Consequently, the time instants t^*, t^{**}, etc. must be approximated with the generic points of the time grid. The choice of $t^* = t$ or $t^* = t + \Delta t$, which are the obvious alternatives, will depend on the marching process used for the integration of the field variables. In this connection it should be pointed out that the model equations allow for the choice of integration procedures in which the inflowing transport terms are evaluated at $t^* = t$, the outflowing terms at $t^{**} = t + \Delta t$ and the impulse terms at $\bar{t} = t + \Delta t/2$.

Equations for a Boundary Cell

It was pointed out earlier that a difficulty inherent in any Eulerian approach is that concerned with the treatment of moving boundaries. If the close-in effects of contained nuclear explosions are simulated by an expanding pressure pulse applied on a spherical cavity, the cavity wall will undergo a continuous expansion such that its position will generally not coincide with the Eulerian grid. Consequently, if the position of the boundary at all times is required, as in the present case, some kind of Lagrangian description must be used at the cavity wall. This can be achieved by introducting a boundary cell of variable geometry, and leaving the treatment of the neighboring interior cells essentially unchanged.

At a generic time after the onset of motion, the cavity wall will lie somewhere between two consecutive grid points, as illustrated in Fig. 3, and the cell in which

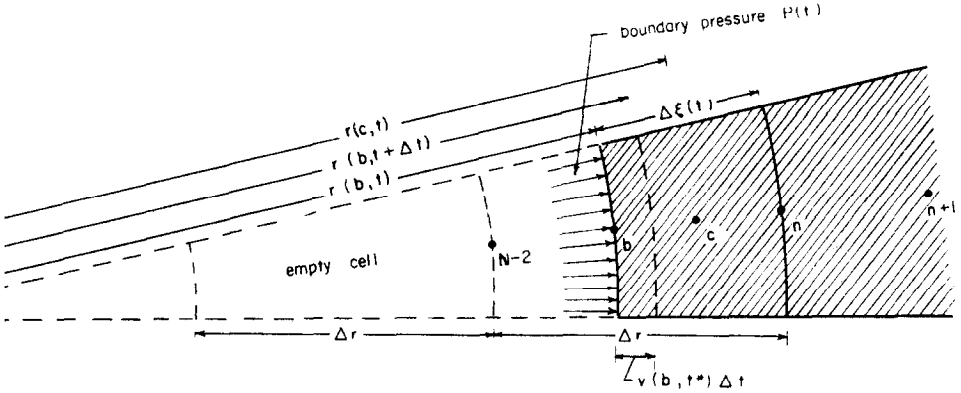

FIG. 3. Boundary cell.

the boundary lies is partially empty. In Fig. 3, n is the first of the fixed reference grids from the boundary, whereas b and c are Lagrangian points moving with the medium inside the boundary cell. In the following, the quantities labeled by b are defined at the cavity wall, whereas the quantities labeled by c refer to the center of the material in the boundary cell. These are the average quantities inside this portion of the variable volume.

If no mass is assumed to flow into the boundary cell from the cavity, the conservation statements for the boundary cell would be

$$M(c, t + \Delta t) = M(c, t) - \Delta M_0(n), \tag{19}$$

$$T(c, t + \Delta t) = T(c, t) - \Delta T_0(n) + \Delta I(c), \tag{20}$$

$$H(c, t + \Delta t) = H(c, t) - \Delta H_0(n) + \Delta W(c). \tag{21}$$

The basic difference with respect to the interior equations is that the volume of the material considered here is no longer constant but changes as a result of the boundary motion.

Assuming that during the time interval Δt the boundary advances from the position $r(n) - \Delta\xi(t)$ to the new position $r(n) - \Delta\xi(t) + v(b, t^*)\Delta t$, the volume of material in the boundary cell, then becomes,

$$\tau(c, t) = r^2(c, t)\,\Delta\xi(t)\,\Delta\varphi\,\Delta\theta \cong r^2(n)\,\Delta\xi(t)\left[1 - \frac{\Delta\xi(t)}{r(n)}\right]\Delta\varphi\,\Delta\theta, \tag{22}$$

and

$$\begin{aligned}\tau(c, t + \Delta t) &\cong r^2(c, t + \Delta t)[\Delta\xi(t) - v(b, t^*)\,\Delta t]\,\Delta\varphi\,\Delta\theta \\ &\cong r^2(n)\,\Delta\xi(t)\left\{1 - \frac{\Delta\xi(t)}{r(n)} - \frac{v(b, t^*)\Delta t}{\Delta\xi(t)}\left[1 - \frac{2\,\Delta\xi(t)}{r(n)}\right]\right\},\end{aligned} \tag{23}$$

where $O(\Delta\xi/r^2)$ and $O(\Delta t^2)$ terms have been neglected.

Substituting Eqs. (22) and (23) into Eqs. (19) and (20), respectively, and computing the outflux and impulse terms exactly as for the interior equations yield

$$\rho(c, t + \Delta t) = [\rho(c, t)\,\Delta\xi(t)\,\eta(t) - m(n, t^{**})\,\Delta t]/[\Delta\xi(t)\,\eta(t) - v(b, t^*)\,\epsilon(t)\,\Delta t] \tag{24}$$

for the conservation of mass, and

$$m(c, t + \Delta t) = \frac{[m(c, t)\,\Delta\xi(t)\,\eta(t) - m^2(n, t^{**})\,\Delta t/\rho(n, t^{**}) + \omega_h(t)]}{[\Delta\xi(t)\,\eta(t) - v(b, t^*)\,\epsilon(t)\,\Delta t]} \tag{25}$$

for the conservation of momentum (with hydrodynamic stress conditions), where

$$\eta(t) = 1 - \frac{\Delta\xi(t)}{r(n)},$$

$$\epsilon(t) = 1 - \frac{2\,\Delta\xi(t)}{r(n)},$$

and, $\omega_h(t) = \{P(\bar{t}) - p(n, \bar{t}) - 2\Delta\xi(t)[P(\bar{t}) - p(c, \bar{t})]/r(n)\}\,\Delta t$. Here, $P(t)$ is the applied boundary pressure. Eq. (25) holds also for nonhydrodynamic stress components, provided ω_h is replaced by

$$\omega_s = \{P(\bar{t}) - \sigma_r(n, \bar{t}) - 2\Delta\xi(t)[P(\bar{t}) - \sigma_\theta(c, \bar{t})]/r(n)\}\,\Delta t.$$

An expression for the conservation of energy can be similarly obtained.

It should now be observed that in Eqs. (24) and (25), the boundary velocity $v(b, t^*)$, a Lagrangian quantity, appears as an extraneous unknown. This quantity

may be determined by extrapolation, which will generally depend on the integration method used in the overall solution process. One possible extrapolation method will be discussed in detail in the next section.

It is interesting to note that, with a slight rearrangement of terms, in the limit as $\Delta t \to 0$ and $\Delta \xi \to 0$, Eqs. (24) and (25), yield

$$v_b = v_r \,, \tag{26}$$

and from $P_b - p_r = \rho_r v_r (v_r - v_b)$,

$$P_b = p_r \tag{27}$$

where the subscript b denotes boundary quantities, and the subscript n denotes quantities at point n of the boundary cell.

These two apparently trivial relationships can be interpreted by considering the cavity wall as a contact discontinuity. Since no influx of mass flow occurs across the boundary, Eqs. (26) and (27) represent a degenerate case of the Rankine–Hugoniot equations.

III. Calculation Procedure

Numerical Analysis

The actual solution of the boundary and interior finite-difference equations of the model requires a stable marching process in the space–time domain. The choice of such a process is not unique. This is especially true for the boundary equations and the extrapolation procedure required to describe the motion of the cavity wall when the boundary velocity is not a prescribed input quantity.

For simplicity, only the hydrodynamic condition is described here. The same numerical method applies also to the nonhydrodynamic case, with one major difference, which will be discussed later.

The marching process involves updating the field quantities from a generic time t (at which all quantities are supposed known) to time $t + \Delta t$. This process consists of two sweeps, the second sweep being essentially an iteration. The computational steps which constitute the first sweep are as follows:

(1) With Eq. (25), and using $t^* = t^{**} = \bar{t} = t$, $m(c, t + \Delta t)$ is calculated for the boundary cell. Similarly, the momentum values of all interior cells, $i \geqslant n + 1$, are updated using Eq. (11) with $t^* = t^{**} = \bar{t} = t$.

In order to enhance the stability properties of Eq. (11) in the presence of shock discontinuities, artificial viscosity terms are added to the pressure terms (to be discussed later).

(2) On the basis of the interpolation formula

$$[r(c, t)/r(n + 1)] = [m(c, t + \Delta t)/m(n + 1, t + \Delta t)]^{\alpha_1}, \tag{28}$$

the decay parameter α_1 is obtained. The momentum at n is then computed as

$$m(n, t + \Delta t) = m(n + 1, t + \Delta t)[r(n)/r(n + 1)]^{\alpha_1}. \tag{29}$$

(3) With the knowledge of $m(n, t + \Delta t)$, the values of ρ at all the interior cells starting from $n + 1$ are updated using Eq. (15) with $t^* = t^{**} = \bar{t} = t + \Delta t$. The corresponding values of p and of the local sound velocity c are obtained from the given pressure-density relationship.

(4) The boundary pressure is a prescribed input quantity; consequently, once loading or unlaoding is specified, p is uniquely determined. Hence, from the function $p = f(\rho)$, the density at the cavity is calculated as,

$$\rho(b, t + \Delta t) = f^{-1}[(Pt + \Delta t)]$$

(5) A value of the decay parameter α_2 is computed from

$$r(b, t)/r(n + 1) = [\rho(b, t + \Delta t)/\rho(n + 1, t + \Delta t)]^{\alpha_2}$$

Using this value of α_2, both $\rho(c, t + \Delta t)$ and $\rho(n, t + \Delta t)$ can be calculated by means of an interpolation equation similar to Eq. (29). The updated velocities for all points, except the boundary point b, are then obtained simply as

$$v(i, t + \Delta t) = m(i, t + \Delta t)/\rho(i, t + \Delta t), \qquad \text{for all} \quad i \geqslant n + 1.$$

(6) The boundary velocity $v(b, t + \Delta t)$ is computed by a least-square linear extrapolation using the values $v(c, t + \Delta t)$, $v(n + 1, t + \Delta t)$ and $v(n + 3, t + \Delta t)$; namely, the values at the center of the first three cells in the same row, including the boundary cell. The weights for $v(c, t + \Delta t)$ and $v(n + 1, t + \Delta t)$ are the masses $M(c, t + \Delta t)$ and $M(n + 1, t + \Delta t)$, whereas the weight for $v(n + 3, t + \Delta t)$ is the mass $M(n + 3, t + \Delta t)$ multiplied by a factor which is inversely proportional to $M(c, t + \Delta t)$; or $1 - M(c, t + \Delta t)/M_0(c, t + \Delta t)$. Here M_0 is the mass contained in the boundary cell before the emptying process began. This scheme is adopted for the following reasons:

(a) The mass in a boundary cell decreases as the cavity expands; consequently the accuracy of $v(c, t + \Delta t)$ may decrease accordingly.

(b) The interpolation and weighing procedure should produce a smooth transition as the cavity expands from an empty cell to a new boundary cell containing its full mass. The above choice of the weights provides the required smoothness.

The above six steps complete the calculations for the first sweep. At this point all the field variables are updated at all the grid points. The second sweep then uses the newly computed values at all the grid points in the same way as an implicit scheme. The calculational steps are exactly the same as for the first sweep, except that Eqs. (25), (11) and (15) are now as follows:

$$m_2(c, t + \Delta t) = \frac{[m(c, t)\,\Delta\xi(t)\,\eta(t) - m_1^2(n, t + \Delta t)\,\Delta t/\rho_1(n, t + \Delta t) + \omega_{h1}(t)]}{[\Delta\xi(t)\,\eta(t) - v(b, t)\,\epsilon(t)\,\Delta t]}, \tag{25a}$$

$$\begin{aligned} m_2(i, t + \Delta t) = m(i, t) + \frac{\Delta t}{\Delta r}\,[&p_1(i - 1, t + \Delta t) + q_1(i - 1, t + \Delta t) \\ &+ m_1^2(i - 1, t + \Delta t)/\rho_1(i - 1, t + \Delta t) \\ &- p_1(i + 1, t + \Delta t) - q_1(i + 1, t + \Delta t) \\ &- m_1^2(i + 1, t + \Delta t)/\rho_1(i + 1, t + \Delta t)] \\ &- \frac{\Delta t}{r(i)}\,[m_1^2(i + 1, t + \Delta t)/\rho_1(i + 1, t + \Delta t) \\ &+ m_1^2(i - 1, t + \Delta t)/\rho_1(i - 1, t + \Delta t)] \\ &+ \frac{\Delta t}{r(i)}\,[p_1(i, t + \Delta t) - p_1(i - 1, t + \Delta t) - p_1(i + 1, t + \Delta t)]; \end{aligned} \tag{11a}$$

where q_1 is an artificial viscosity term.

$$\begin{aligned} \rho_2(i, t + \Delta t) = \rho(i, t) + \frac{\Delta t}{\Delta r}\,&[m_2(i - 1, t + \Delta t) - m_2(i + 1, t + \Delta t)] \\ &- \frac{\Delta t}{r(i)}\,[m_2(i - 1, t + \Delta t) + m_2(i + 1, t + \Delta t)]. \end{aligned} \tag{15a}$$

Here the subscript 1 is used to denote the quantities obtained at the end of the first sweep, whereas the subscript 2 refers to the final quantities for time $t + \Delta t$.

Once the final value $v_2(b, t + \Delta t)$ is computed, the position of the boundary with reference to point n can be updated using

$$\Delta\xi(t + \Delta t) = \Delta\xi(t) - v_2(b, t + \Delta t)\,\Delta t.$$

If $\Delta\xi(t + \Delta t) \leqslant 0$, it means that the boundary cell has been completely emptied; in this event $\Delta\xi = \Delta r$ is set for the next cycle of computation and the boundary cell is automatically advanced to the next cell of the same row.

No artificial viscosity terms were used in Eqs. (25) and (25a) since this was found to yield a stable behavior of the solution near the cavity.

Certain modifications are required in the treatment of the boundary when a nonhydrodynamic stress condition is considered. First of all, the computational scheme must permit the calculation of both the mean pressure and the stress deviator at the cavity wall. These two stress components must necessarily be distinguished in order to allow the determination of the material density at the boundary from the given p–ρ relationship. For this purpose it is assumed that the ratio of the mean pressure to the calculated radial stress at the cavity is the same as that of the first interior cell, which has been obtained from the previous cycle of computation.

Once the boundary values of the pressure and stress deviator are determined at the beginning of each time step, the procedure described above for the hydrodynamic case remains valid when the appropriate momentum equations are used. The deviatoric stresses $s_r(c, t + \Delta t)$ and $s_r(n + 1, t + \Delta t)$ are interporlated using the boundary value and the corresponding deviator of the first interior cell $s_r(n + 1, t + \Delta t)$ through an equation similar to Eq. (29). The stress deviators of the interior cells are computed from the velocities and the material moduli through an appropriate constitutive relationship.

Truncation Error and Stability

Questions of stability arise from the use of Eqs. (11) and (15) in Steps (1) and (3) of the first sweep of the computational algorithm. If $\bar{m}$ and $\bar{\rho}$ represent an exact solution of Eqs. (13) and (17), a Taylor expansion about the point (i, t) will show that the truncation errors of Eq. (11) (with viscosity terms q added) with $t^* = t^{**} = \bar{t} = t$ is

$$\frac{\partial q}{\partial r} + \frac{1}{2}\frac{\partial^2 \bar{m}}{\partial t^2}\Delta t + O(\Delta r^2).$$

Likewise, the corresponding truncation error of Eq. (15) with $t^* = t^{**} = \bar{t} = t + \Delta t$, is

$$\left(\frac{1}{2}\frac{\partial^2 \bar{\rho}}{\partial t^2} + \frac{\partial^2 \bar{m}}{\partial r \partial t} + \frac{2}{r}\frac{\partial \bar{m}}{\partial t}\right) + O(\Delta r^2).$$

If the integration scheme is stable, the truncation errors arising from the finiteness of Δt are likely to be much smaller than the errors arising from the finiteness of Δr. In practice, the choice of Δr is dictated by the storage capacity and the speed of a computer. Consequently, the space mesh is invariably coarser then the time mesh. Therefore, aside from the diffusion term $\partial q/\partial r$, the dominant truncation error terms are of order $O(\Delta r^2)$. This is a direct consequence of the centered difference

formulation of the transport terms in the model equations. The scheme considered here does not require any more stringent stability requirements than other differencing schemes [8].

A linear stability analysis of the interior difference equations is outlined below; this is intended primarily to show the need for artificial viscosity terms. The relevant equations to be analyzed are the following:

$$\begin{aligned} m(i, t + \Delta t) = m(i, t) + \frac{\Delta t}{\Delta r}\,[&p(i-1, t) + q(i-1, t) + m^2(i-1, t)/\rho(i-1, t) \\ &- p(i+1, t) - q(i+1, t) - m^2(i+1, t)/\rho(i+1, t)] \\ &+ \frac{\Delta t}{r(i)}\,[m^2(i-1, t)/\rho(i-1, t) + m^2(i+1, t)/\rho(i+1, t)] \\ &+ \frac{\Delta t}{r(i)}\,[2p(i, t) - p(i-1, t) - p(i+1, t)]; \end{aligned} \tag{30}$$

and

$$\begin{aligned} \rho(i, t + \Delta t) = \rho(i, t) + \frac{\Delta t}{\Delta r}\,&[m(i-1, t + \Delta t) - m(i+1, t + \Delta t)] \\ &- \frac{\Delta t}{r(i)}\,[m(i-1, t + \Delta t) + m(i+1, t + \Delta t)], \end{aligned} \tag{31}$$

in which Eq. (30) is obtained from Eq. (11) for $t^* = t^{**} = \bar{t} = t$ by adding the terms $q(i, t)$, and Eq. (31) is Eq. (15) for $t^* = t^{**} = \bar{t} = t + \Delta t$. The artificial viscosity is taken as in [8],

$$q(i, t) = B\rho(i, t)\, c(i, t)[m(i-1, t)/\rho(i-1, t) - m(i+1, t)/\rho(i+1, t)],$$

where B is a constant to be determined by numerical experiment. Stability may be analyzed by first obtaining the linearized equations of the first variation of Eqs. (30) and (31) (see Chap. 5 of Ref. [9]) and then testing the local time growth of a test solution in the form of a Fourier component as suggested by von Neumann for linear equations. It can thus be shown that the amplification factors g of the equations of first variation satisfy

$$\begin{aligned} g^2 + [i\mu Av(2 + \mu BA^2c) + \mu BA^2c + \mu^2A^2(c^2 - v^2) - 2]\, g \\ + 1 - 2i\mu Av - \mu BA^2c = 0, \end{aligned} \tag{32}$$

where

$$i = \sqrt{-1}; \qquad A = 2 \sin k; \qquad \text{and} \quad \mu = \Delta t/\Delta r.$$

The soundspeed c and the velocity v are regarded as locally constant quantities Von Neumann's criterion predicts local stability if $| g | \leqslant 1$. Now let

$$\mu A v = M; \qquad \mu A^2 B c = Q; \qquad (c^2 - v^2)\,\mu A^2 - 2 = K,$$

and,

$$\beta_1 = [M^2(2 + Q)^2 + (K + Q)^2]^{1/2}; \qquad \beta_2 = [4M^2 + (1 - Q^2)^2]^{1/2}.$$

An algebraic criterion for finding upper bounds to the moduli of the roots of an equation containing complex coefficients [10], says that $| g | \leqslant 1$ if the inequalities.

$$1 - \beta_1 - \beta_2 > 0, \tag{33}$$

$$1 - \beta_1 > 0, \tag{34}$$

are both satisfied. It should be emphasized that if $B = 0$, no value of M and K can satisfy the inequality of Eq. (33). This means that stability of Eqs. (30) and (31) cannot be assured if no artificial viscosity terms are used.

Implicit in the equations under consideration is the assumption that $v^2/c^2 \ll 1$. Under this condition the inequalities of Eqs. (33) and (34) lead to the following stability requirements,

$$c\,\Delta t/\Delta r < \sqrt{2}/2, \tag{35}$$

and

$$c\,\Delta t/\Delta r < (B^2 + 3)^{1/2}/2 - B/2. \tag{36}$$

For example, if $B = 0.5$, Eq. (36) yields

$$c\,\Delta t/\Delta r < 0.65 < \sqrt{2}/2.$$

For problems involving shock propagation, stability analysis is of little value. For these situations, the following inequality [9]

$$(c + U)\,\Delta t/\Delta r < 1 \tag{37}$$

where U is the shock velocity, is used as a guide.

Stability requirements for the equations of the second sweep are not discussed. Numerical evidence show that, if the calculations of the first sweep are stable, the iteration performed in the second sweep is also stable.

IV. Applications

Comparison with Analytic Solution for Small Deformation

An exact solution for the propagation of an elastic shock wave generated by the quasi-static expansion of a gas in a spherical cavity is given in Ref. [11]. The solution is valid only for linearly elastic materials and for small displacements. The cavity is assumed to be filled with a gas and the pressure $P(t)$ is given by

$$P(t) = P_0[1 - 3\gamma u(a, t)/a], \tag{38}$$

where P_0 is the initial pressure, γ is the ratio of specific heat, and $u(a, t)$ is the radial displacement of the cavity of initial radius a.

The present calculations were performed assuming zero shear modulus, i.e. a hydrodynamic state of stress, and a bulk-type elastic law

$$p = K\left(\frac{\rho}{\rho_0} - 1\right) \tag{39}$$

was used, in which K is the bulk modulus. The following values were assigned for the parameters in the present problem:

$$P_0 = 4 \text{ ksi}; \quad \gamma = 5/3; \quad a = 20 \text{ in.}; \quad K = 5235 \text{ ksi}; \quad \rho_0 = 2.67 \text{ gm/cm}^3.$$

A plot of the velocity-histories at the cavity and at $r = 50$ in., during the first millisecond, is shown in Fig. 4. It should be realized that the comparison between the exact and the numerical solution is meaningful only for the early time of up to approximately 0.5 or 0.6 msec. As the velocities (and the displacements) grow larger than a certain limit, the analytic solution, which is based on the assumption of small deformations and constant density, is bound to yield lower values than the present numerical solution, which is based on the assumption of a hydrodynamic flow. Up to about 0.5 msec., a progressive refinement of the mesh size from 4 to 0.5 in. clearly shows the convergence of the numerical results to the exact solution. The convergence is particularly significant for the cavity velocity, which is calculated by extrapolation from the interior field. Since the gradient of velocity is steep in the neighborhood of the cavity, as may be seen from Figs. 5 and 6, the present problem constitutes a rather severe test for the proposed treatment of the boundary.

The spatial distribution of the velocities is shown at two different times, $t = 0.5$ and $t = 1.0$ msec. in Figs. 5 and 6, respectively. Figure 5 shows that significant errors occur only at the shock front; this is a result of the smoothing effect of the viscosity terms. However, since the particle-velocities at the shock front are much smaller than the peak velocities found at the cavity, this error appears to be negligible.

The above results were obtained using linear viscosity terms, as given by Eq. 32, with $B = 0.5$. A constant time step determined by the condition

$$\frac{c\,\Delta t}{\Delta r} = 0.2 \qquad [c = (K/\rho_0)^{1/2}]$$

was found to be quite satisfactory.

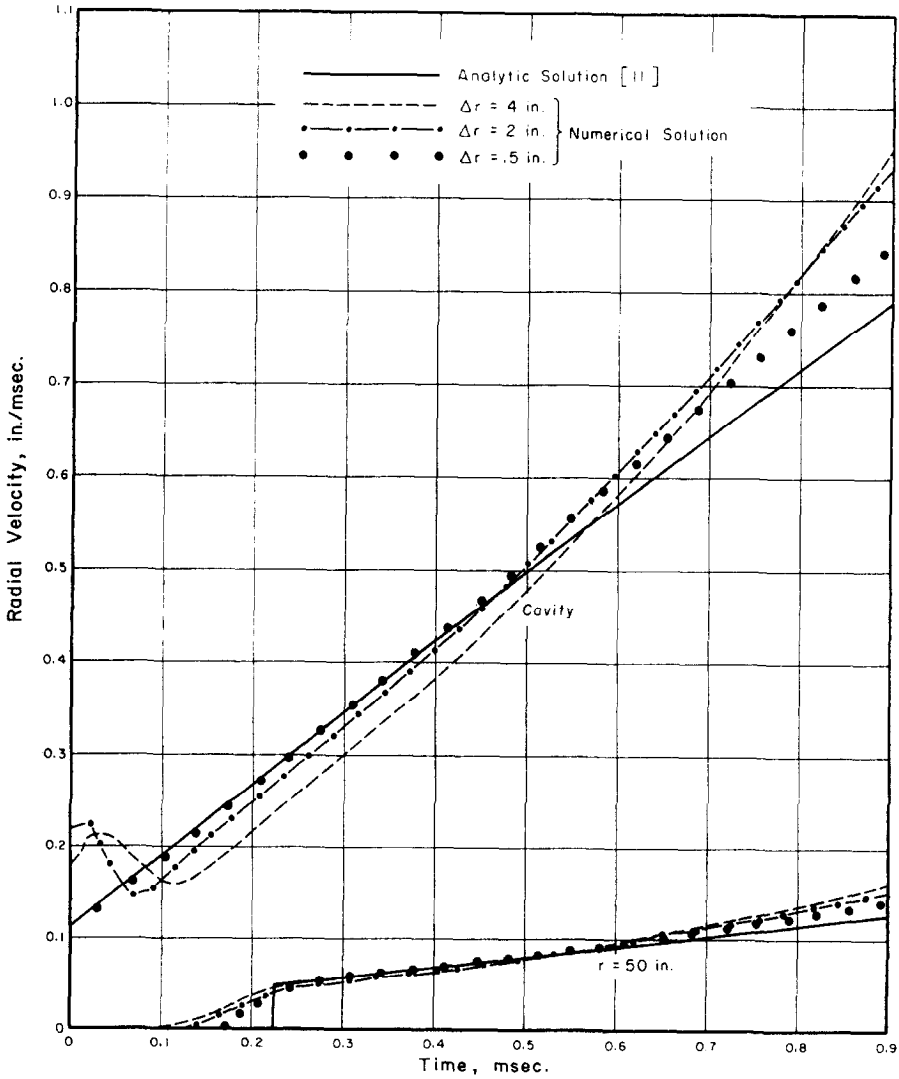

FIG. 4. Velocity histories at cavity and at $r = 50$ in.

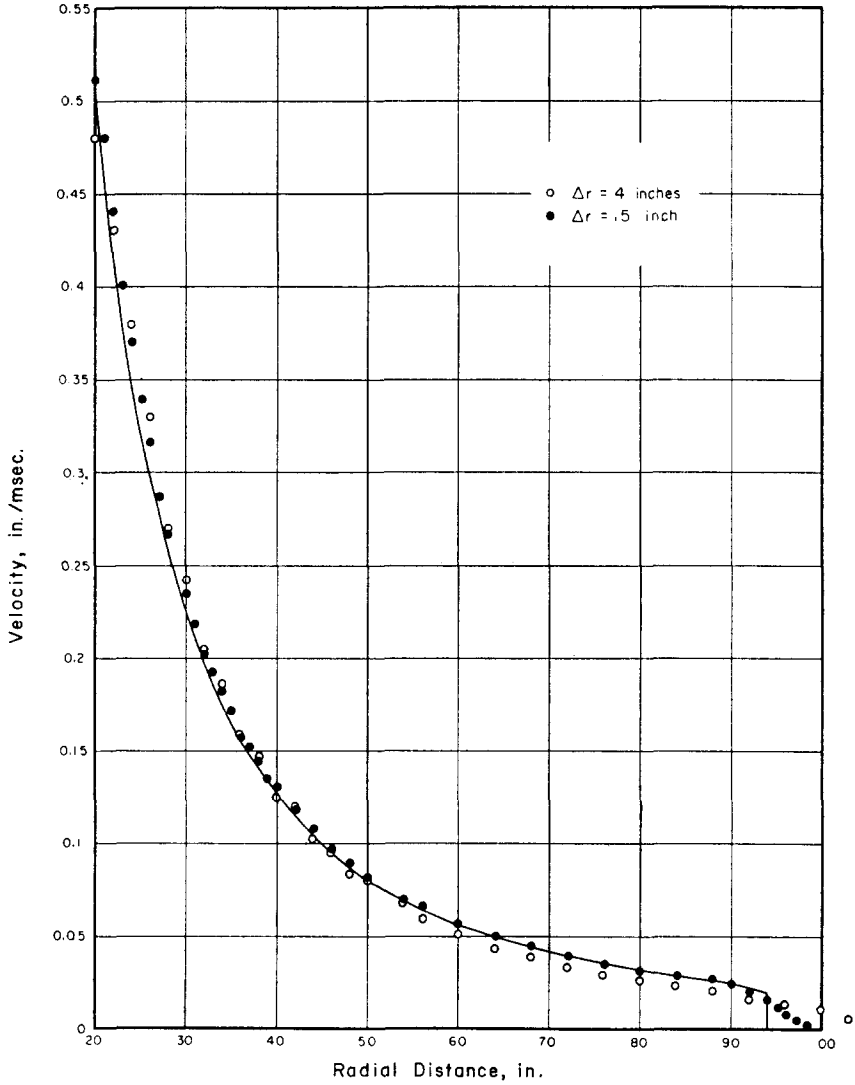

FIG. 5. Velocity profile at $t = 0.50$ msec.

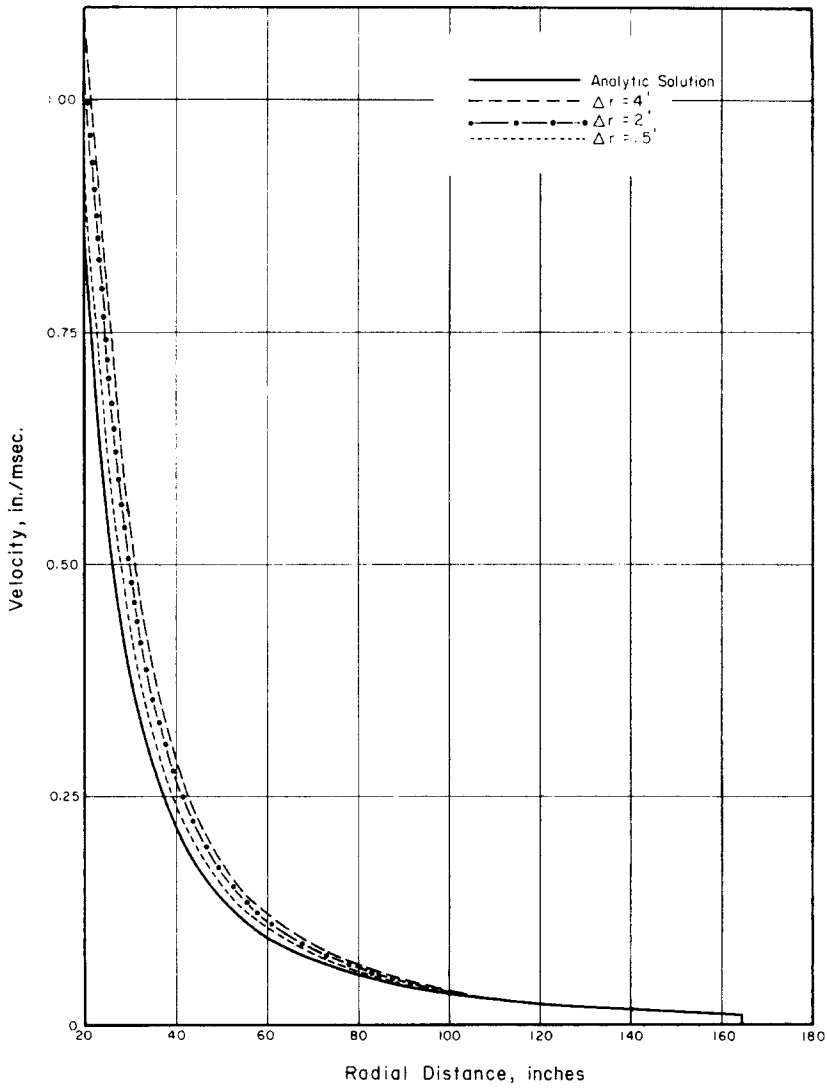

FIG. 6. Velocity profile at $t = 1.0$ msec.

Elastic-Plastic Wave Propagation in Granite

The second application is concerned with the calculation of ground motion in the low stress region of the Hardhat experiment, which is a 5-kiloton nuclear explosion in granite that took place at a depth of 950 ft at the Nevada Test Site. Because a number of particle acceleration and velocity measurements were obtained, the Hardhat experimental data provide a good basis for evaluating the validity of the numerical calculations. Detailed descriptions of the data and their sources can be found in Refs. [12] and [13].

A nonhydrodynamic stress description is assumed with $\sigma_r = -p + s_r$ and $\sigma_\theta = -p - s_r/2$, where $s_r = 2(\sigma_r - \sigma_\theta)/3$ is the stress deviator for a spherically symmetric problem. In the stress levels of interest, which are below 4 kilobars (= 58 ksi), the flow may be regarded as isentropic. Thus, it is adequate to assume a linear pressure-density relationship as given by Eq. (39). A bulk modulus $K = 361$ kilobars $= 5235$ ksi and a shear modulus $G = 315$ kilobars $= 4570$ ksi were chosen. With these values the dilatational c and shear c_s velocities calculated on the basis of the elastic relationships

$$c^2\rho_0 = K + \frac{4}{3}G, \qquad c_s^2\rho_0 = G,$$

where $\rho_0 = 2.67$ gm/cm^3 is the initial density of granite, agree with the *in-situ* seismic measurements of 17,580 fps and 10,000 fps, respectively.

Two sets of calculations were performed. In the first set the deviatoric stress is governed by the equations of Grigorian [14]; namely, the yield level is a function of the pressure and the associated flow rule is elastic-perfectly plastic. For a spherically symmetric state of stress, the yield criterion can be written as

$$s_r^2 = F(p) = \frac{4}{3}(\alpha p + b)^2, \tag{40}$$

in which α and b are experimentally determined constants, and the elastic-plastic flow rule is

$$\frac{ds_r}{dt} + \lambda s_r = \frac{4G}{3}\left(\frac{\partial v}{\partial r} - \frac{v}{r}\right), \tag{41}$$

where

$$\lambda = \frac{2Gs_r\left(\dfrac{\partial v}{\partial r} - \dfrac{v}{r}\right) - F'(p)\dfrac{dp}{dt}}{2F(p)}$$

is a plastic multiplier. The deviatoric stress is plastic only when Eq. (40) is satisfied and $\lambda > 0$. For granite $\alpha = 0.895$ and $b = 0.5$ ksi were assumed.

The second set of calculations makes use of the same elastic law, i.e. Eq. (41) with $\lambda = 0$, but with a von Mises' yield criterion. The latter implies that when plastic flow commences, the stress deviator assumes a constant value

$$s_r^p = -2k_0/3,$$

where k_0 is a plastic modulus. The value $k_0 = 3$ kilobars (= 43.5 ksi) was assumed for the persent calculations. It was further hypothesized for both sets of calculations that the medium cannot withstand tensile stresses higher than 1 ksi and that, when this limit is exceeded by σ_r or σ_θ, $G = 0$. If only radial cracks develop, it might be more realistic to assume a uniaxial state of stress in the cracked region, with $\sigma_\theta = 0$. This would imply that, in the cracked state, the rock is subdivided into long columns, each of them subjected to purely axial stress [15]. However, such columns are likely to be very thin and, therefore, to be easily crushed after their formation. For this crushed state, the assumption of a purely isotropic stress state may not be unreasonable.

The calculations were started at 200 ft from the center of the explosion and this distance was taken as the initial radius of the cavity for the model. A pressure pulse of the form

$$P(t) = \frac{P_{\max}}{t_r} te^{1/2[1-(t/t_r)^2]} \tag{42}$$

is applied at the cavity, with $p_{\max} = 4$ kilobars and $t_r = 2$ msec. This approximately represents the smooth pressure-history measurement that was made at the station $r = 203$ ft [16].

The logarithmic attenuation of the peak radial stress with distance, scaled to 5 kilotons in accordance with the usual cube-root law, is illustrated in Fig. 7. The attenuation corresponding to Eq. (40), which is an approximation of the Coulomb–Mohr failure criterion, plots essentially as a straight line in which the peak stress falls off approximately as $r^{-2.03}$. It may be observed that in the analytic curve obtained by Bishop [12], the stresses attentuate at r^{-2}. It may be observed that the results obtained by Butkovich [17] using a Lagrangian approach seems to lie definitely above the experimental data. When plastic flow is governed by Eqs. (40) and (41), it is found that the material yields at very low stress levels and that plastic dissipation is present over the entire region of the calculations; that is, up to a distance of about 760 ft. This may be contrasted with the von Mises case, for which plastic dissipation vanishes below the assumed yield limit of 3 kilobars. This stress level corresponds to a range of approximately 230 ft; beyond this distance the propagation, therefore, is entirely elastic.

The difference in the results obtained with the two different yield criteria are better illustrated by the spatial stress profiles of Fig. 8 and by the radial stress

histories of Fig. 9. The von Mises hypothesis leads to the formation of radial cracks immediately following the main pulse when the propagation becomes elastic; this is caused by tangential stresses exceeding the assumed tensile strength of granite. The radial stress profiles of Fig. 8 shows that the transition from the cracked to the intact region occurs with an abrupt jump; a recent theoretical

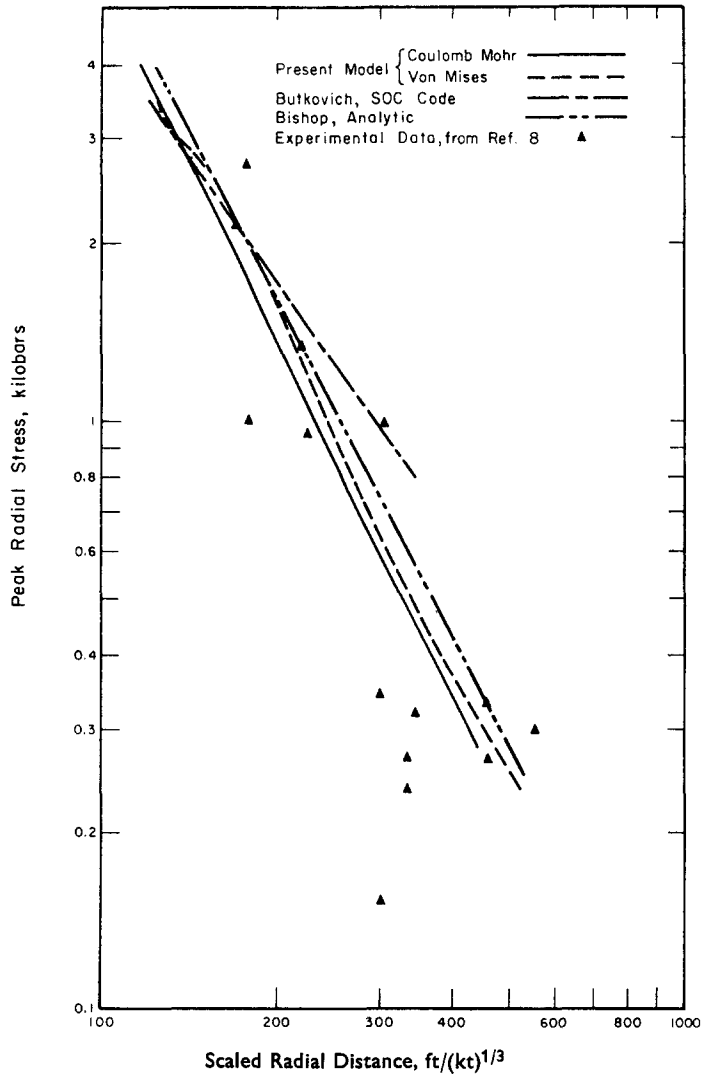

FIG. 7. Radial stress decay in granite (hardhat).

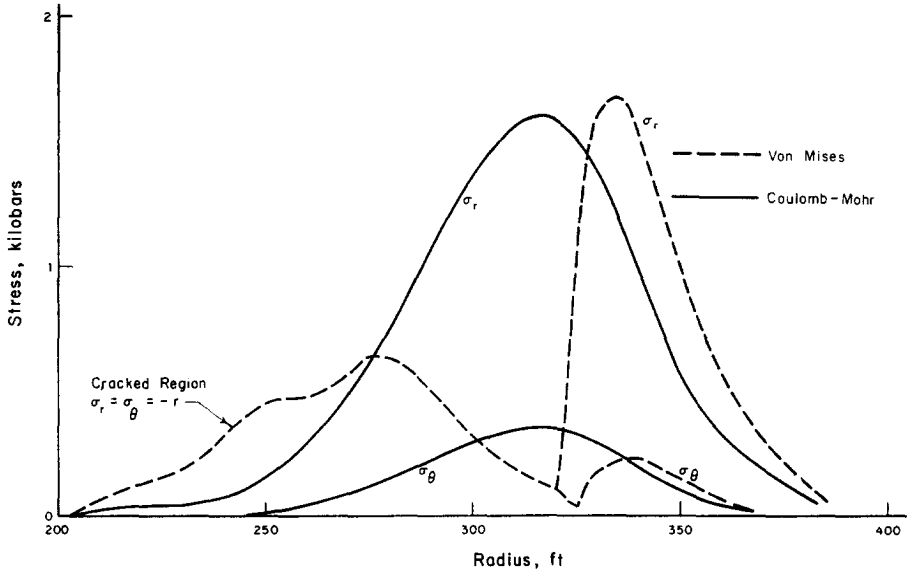

FIG. 8. Stress profiles in granite at $t = 9.05$ msec.

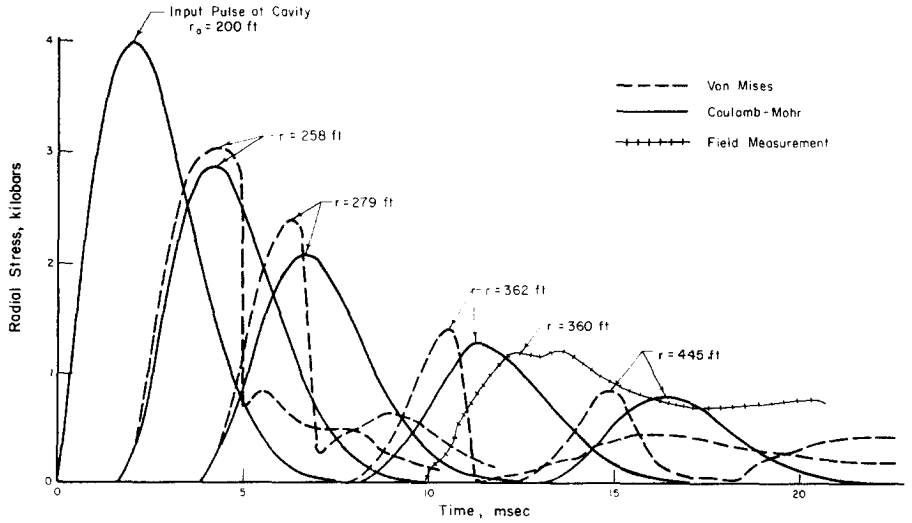

FIG. 9. Radial stress histories in granite.

analysis by Grigorian [17] actually demonstrates that, in a similar problem, the cracked front propagates like a rarefaction shock, traveling at a subsonic speed. The numerical results presented here confirm this prediction and show that the rarefaction front is correctly propagated by the artificial viscosity terms. No cracks arise when Eqs. (40) and (41) are used because in this case the tensile stresses that are developed are practically negligible. It should also be observed from Fig. 9 that the difference in the time of arrival of pulses becomes rather significant at the larger distances (almost 2 msec at 445 ft). The discrepancy in the arrival time between the calculated and observed pulses at 360 ft (see Fig. 9) may be attributed to an error in the determination of the correct position of the instrument [16]; the agreement in the rise times and peak stresses with the measured values is otherwise good.

For this group of calculations a mesh length of 20 in. and linear viscosity terms with $B = 0.2$ were used. The time increment Δt was chosen such that

$$\frac{c\,\Delta t}{\Delta r} = 0.3.$$

Shock Wave Propagation in Playa Silt

The last application described in this study is concerned with the propagation of shock waves resulting from the compressibility or compaction of a granular medium. For this purpose, the properties of a typical soil from the Nevada Test Site, known as playa silt are used. A number of static and dynamic confined uniaxial tests on playa silt, for pressures up to about 1.5 kilobars (= 22 ksi), were performed by Hendron and Davisson [18]. From these data it is possible to obtain pressure-density curves corresponding to the indicated stress level. A typical curve chosen for this purpose is shown in Fig. 10. The dashed lines show the possible unloading paths; in the lower pressure region loading and unloading are assumed to follow the same path, in accordance with the assumptions of Grigorian's theory [14]. The curve of Fig. 10 is related to a specimen with a relatively high initial water content (17.3 %), which explains the rapid attainment of complete compaction and the very steep slope in the upper range. Assuming a density at rest, $\rho_0 = 1.69$ gm/cm^3, this slope corresponds to a sound velocity of approximately 3300 fps, which is close to that corresponding to the compressibility of water. For computational purposes, the lower portion of the curve was approximated by means of a fifth degree polynomial, such as to give a smooth and continuous slope throughout. Also, the straight portion of the curve was extrapolated with a constant slope up to about 30 ksi.

Given the small shear rigidity of the material, a hydrodynamic stress description was adopted.

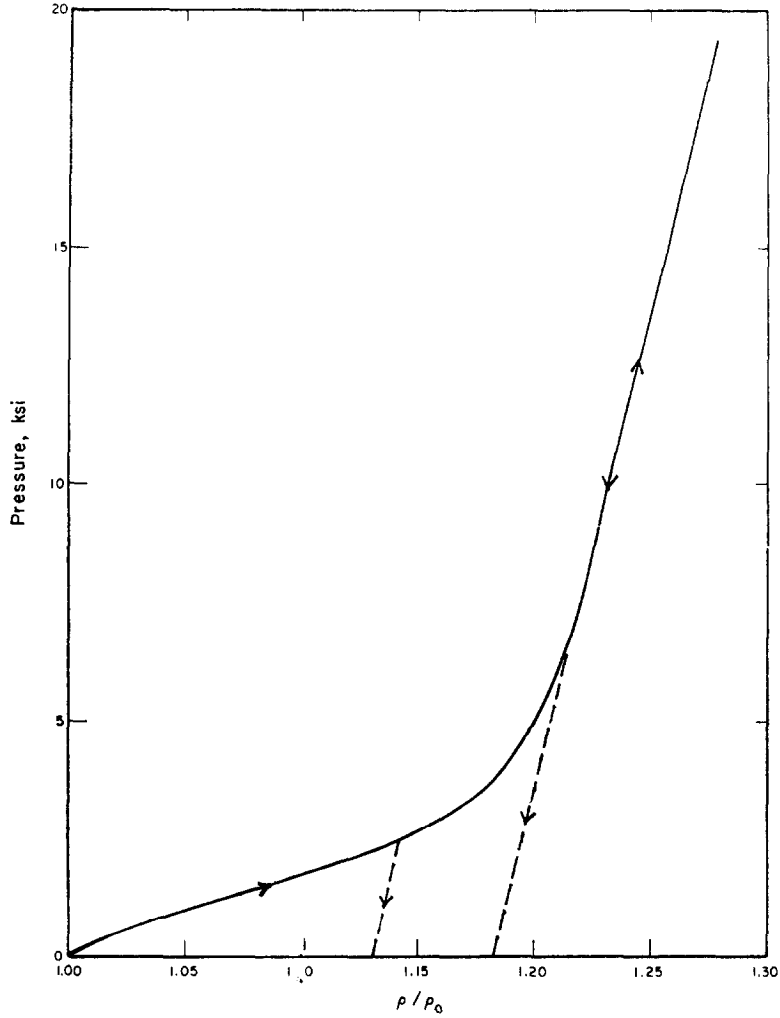

FIG. 10. Pressure-density curves for playa silt.

An initial cavity radius of 5000 in. is assumed and the initial cavity pressure is specified by Eq. (42) with $p_{max} = 30$ ksi (2.07 kilobars) and $t_r = 10$ msec. The space mesh Δr was selected such as to define a shock over a reasonably small zone. Using the linear viscosity terms of Eq. (32), with $B = 0.4$, the effective shock thickness is spread over 3 mesh lengths; thus, a value $\Delta r = 10$ in. was found to provide an acceptably fine description of the jumps. However, differences in the time of arrival of the signals were detected by varying Δr from 5 to 20 inches. This is clearly shown by the velocity-histories of Fig. 11 and by the shock and precursor

paths of Fig. 12. The difference in the arrival times of the presursor signal for $\Delta r = 5$ in. and $\Delta r = 20$ in. is about 2 milliseconds. This indicates that large mesh sizes may produce an unacceptable diffusion of the signals.

A special group of calculations was performed with the purpose of comparing the relative effectiveness of linear vs. quadratic artificial viscosity terms. The quadratic terms used were of the von Neumann–Richtmyer type, or

$$q(i, t) = \tfrac{1}{2}a^2[\rho(i, t) + \rho(i, t - \Delta t)][m^2(i + 1, t)/\rho(i + 1, t) - m^2(i - 1, t)/\rho(i - 1, t)],$$

and $a = 1.6$ was selected after some numerical experiments. The pressure profiles obtained with the two types of viscosity are compared in Fig. 13. The viscosity

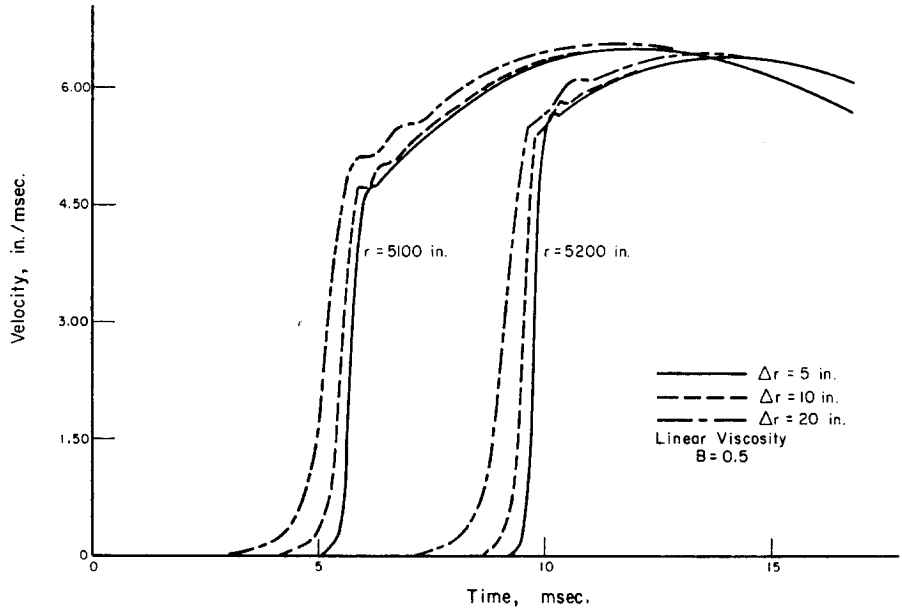

FIG. 11. Effect of mesh size on velocity-histories

terms were used during both loading the unloading and a mesh length of 20 inches was used. It is evident from Fig. 13 that the quadratic terms do not provide sufficient damping for the oscillations immediately behind the shock, whereas the linear terms yield remarkably smoother profiles without causing a significant erosion of the jump. Subsequent calculations were, therefore, performed with linear viscosity terms and $B = 0.5$. Since the shock velocity U is practically constant (approxi-

mately 26.5 in/ms) over a large range and lower than the highest sound velocity attainable in the medium, a time step determined by the condition

$$(c + U)\frac{\Delta t}{\Delta r} = 0.3 \tag{43}$$

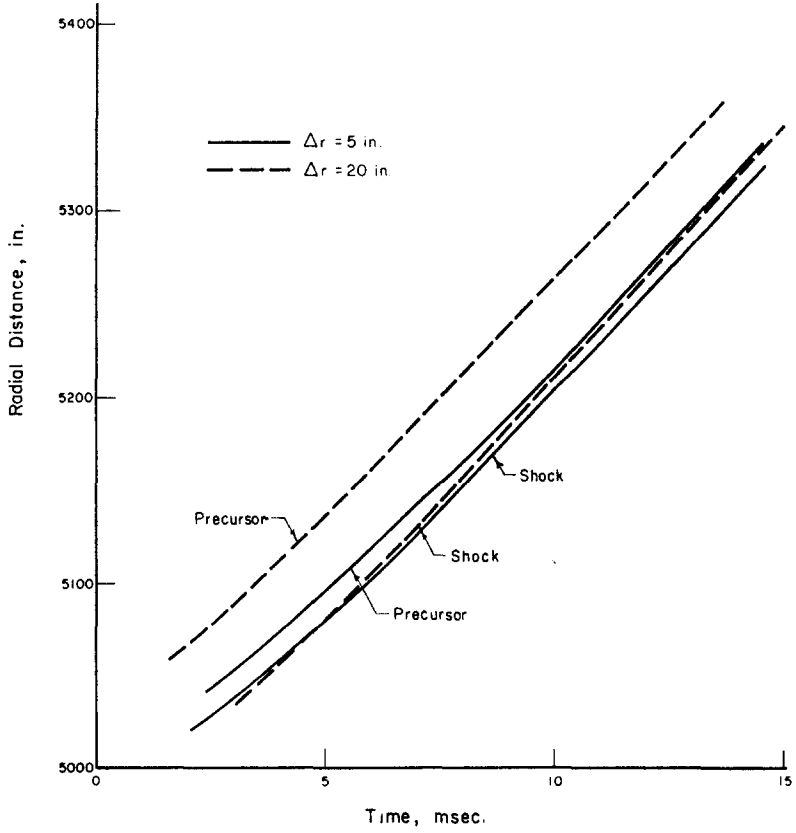

FIG. 12. Shock and precursor paths for varying Δr.

was found adequate. The results of the final calculations are plotted in Figs. 14 through 17. The time-histories of particle velocities and pressures at $r = 5105$ in. and $r = 5205$ in. shown in Figs. 14 and 15, respectively, are discontinued when these locations are reached by the expanding cavity. It should be observed from Fig. 16 that, at later times the peak velocities no longer occur at the jump but at the cavity.

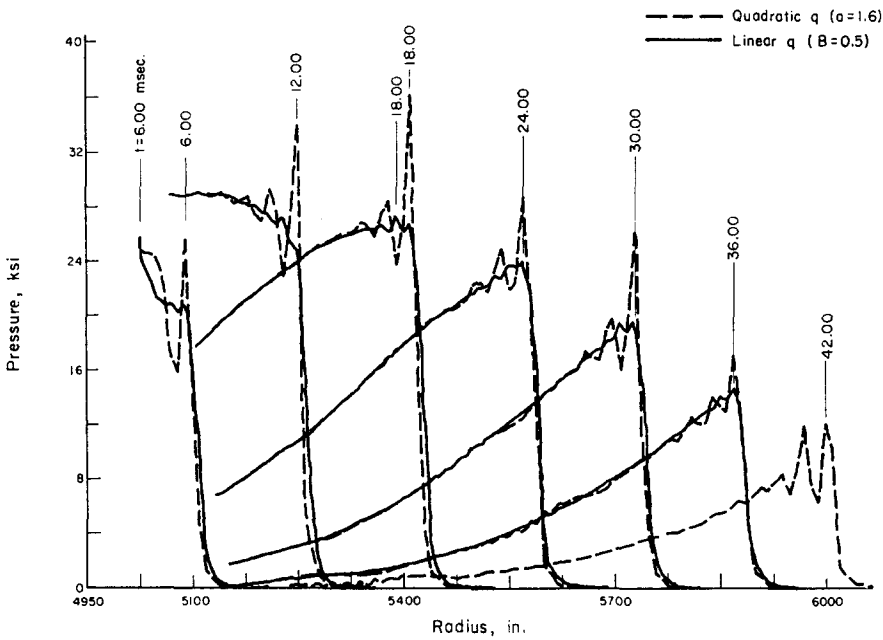

FIG. 13. Comparison between linear and quadratic viscosity effects

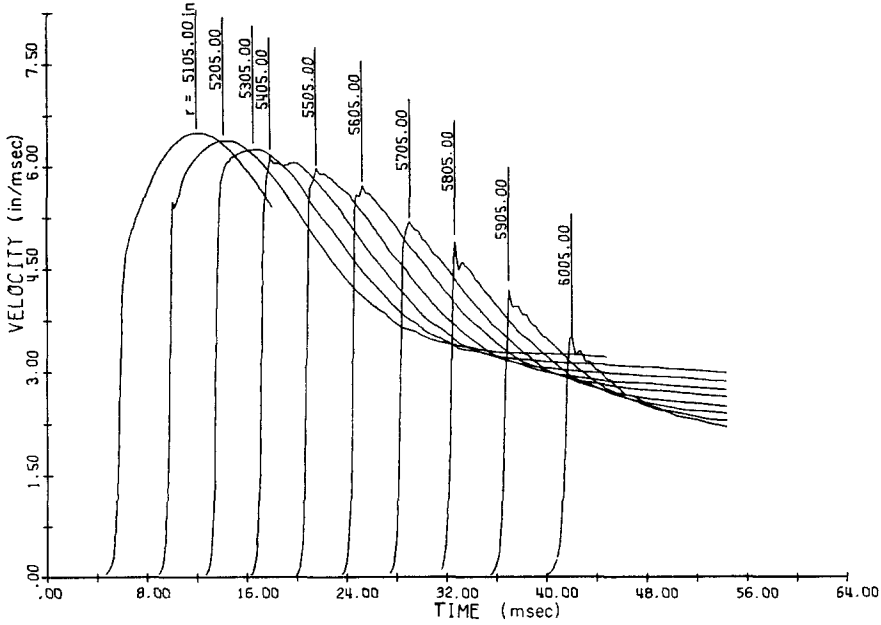

FIG. 14. Velocity histories (playa silt).

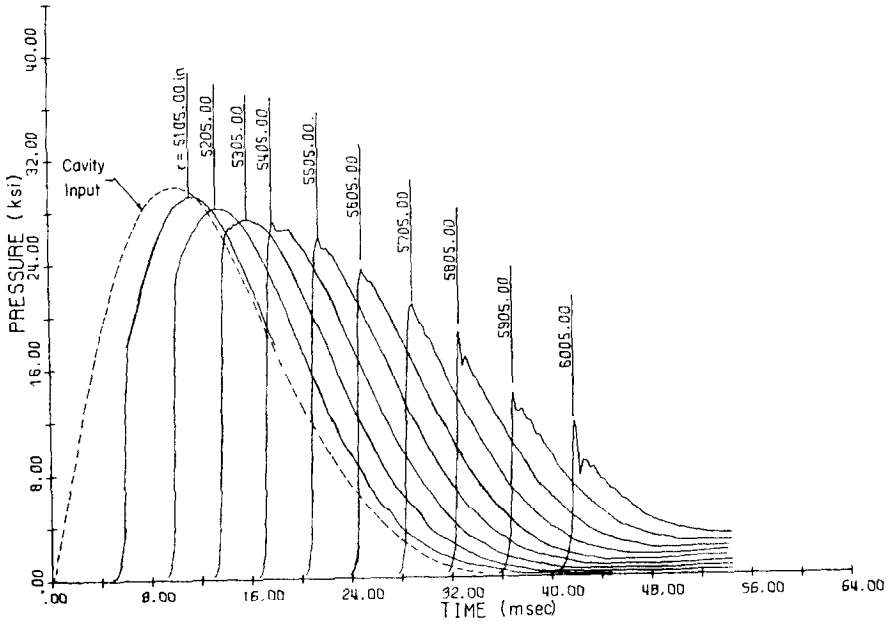

FIG. 15. Pressure histories (playa silt).

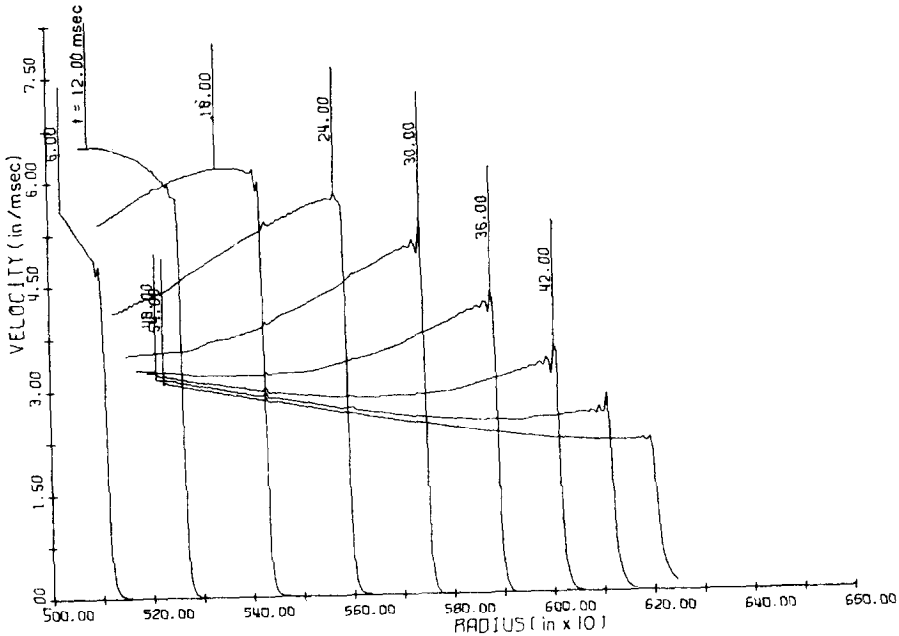

FIG. 16. Velocity profiles (playa silt).

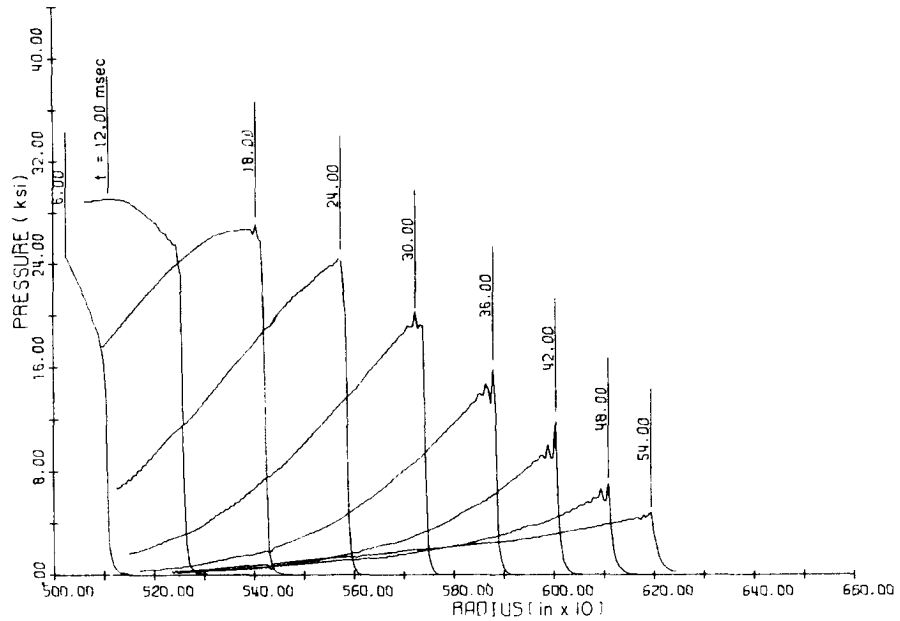

FIG. 17. Pressure profiles (playa silt).

The above results were obtained using the viscosity terms in loading only; namely

$$q(i, t) \neq 0, \qquad \text{when} \qquad v(i-1, t) - v(i+1, t) > 0,$$
$$q(i, t) = 0, \qquad \text{otherwise.}$$

These results illustrate the smoothness of the solutions obtained with the proposed scheme.

V. CONCLUSIONS

The discrete Eulerian model described here is useful for a centered finite difference formulation of the conservation equations of continuum mechanics. A computational scheme for treating the initial-boundary-value problems of an expanding spherical cavity is proposed. However, the associated stability analysis is limited only to the equivalent initial-value problem. Convergence is illustrated with specific calculations.

Numerical solutions obtained for a number of problems indicate that the results are smooth and devoid of "noise" that has generally plagued other numerical schemes.

References

1. P. D. Lax, *Commun. Pure Appl. Math.* **7**, 159–193 (1954).
2. A. H.-S. Ang, "Numerical Approach for Wave Motions in Nonlinear Solid Media." Proc. Conf. on Matrix Methods in Structural Mechanics, Wright-Patterson AFB, Nov. 1966, 753–777.
3. W. E. Johnson, OIL, "A Continuous Two-Dimensional Eulerian Hydrodynamic Code." General Atomic Report GAMD-SS80, January 1965.
4. W. F. Noh, "CEL: A Time Dependent, Two Space Dimensional, Coupled Eulerian–Lagrangion Code." Report No. UCRL–7465, Univ. of California, LRL, August 1963.
5. C. S. Godfrey, D. J. Andrews *et al.*, "Calculation of Underground and Surface Explosions." Report No. AFWL-TR-56-211, Air Force Weapons Lab., June 1966.
6. M. Rich, "A Method for Eulerian Fluid Dynamics." Report No. LAMS-2826, Los Alamos Scientific Laboratory, March 1963.
7. F. G. P. Seidl, "SOC—A Numerical Model for the Behavior of Materials etc." Report No. UCID-5033, Univ. of Cal., July 1965.
8. A. G. Gentry, E. M. Martin, and B. J. Daly, *J. Comp. Phys.* **1**, 87–118 (1966).
9. R. D. Richtmyer, K. W. Morton, "Difference Methods for Initial-Value Problems." 2nd Edition, Interscience, New York (1967).
10. J. V. Uspensky, "Theory of Equations." McGraw-Hill, New York (1948).
11. H. F. Cooper, "Generation of an Elastic Wave by Quasi-Static Isentropic Expansion of a Gas in a Spherical Cavity etc." Report No. AFWL-TR-66-83, Air Force Weapons Laboratory, September 1966.
12. R. H. Bishop, "Spherical Shock Waves from Underground Explosions," *in* "Close-in Phenomena of Buried Explosions." Report No. DASA-1382, Sandia Corporation, May 1963.
13. F. M. Sauer, "Ground Motion from Underground Nuclear Explosions," *in* "Nuclear Geoplosics, Part 4: Empirical Analysis of Ground Motion and Cratering" Report No. DASA-1285 (IV).
14. S. S. Grigorian, *Prikl. Math. Mekh.* **24**, 1057–1072 (1960).
15. S. S. Grigorian, *Prikl. Math. Mekh.* **31**, 643–669 (1967).
16. Heusinkfeld *et al.*, "Stress History Measurements with Piezoelectric Crystals." Hardhat Preliminary Report, Project 26.21, K Div. LRL, 1962.
17. T. R. Butkovich, "Calculation of the Shock Wave from an Underground Nuclear Explosion in Granite." Proc. 3rd Plowshare Symposium, Report No. AEC TID-7695, Univ. of California LRL 1964.
18. A. J. Hendron and M. T. Davisson, "Static and Dynamic Behavior of a Playa Silt in One-Dimensional Compression." Report No. RTD TDR-73-3078, 1963.